A new method for estimating NO_x emissions and lifetimes from satellite observations

Steffen Beirle[1] and Thomas Wagner[1]

[1]Satellitenfernerkundung, Max-Planck-Institut für Chemie, Mainz, Germany

Corresponding author: Steffen Beirle (steffen.beirle@mpic.de)

Abstract. We present a new method for estimating NO_x emissions and effective lifetimes from large cities based on NO_2 measurements from TROPOMI (PAL dataset, May 2018-November 2021). As in previous studies, the estimate is based on the downwind plume evolution for different wind directions separately. The novelty of the presented approach lies in the simultaneous fit of downwind patterns for opposing wind directions, which makes the method far more robust (i.e. less prone to local minima with nonphysically high or low lifetimes) than a single exponential decay fit. In addition, the new method does not require the assumption of a city being a "point source", but derives also the spatial distribution of emissions.

The method was successfully applied to 100 cities worldwide on seasonal scale. Fitted emissions generally agree reasonably with EDGAR v6 (R=0.72) and are on average 14% lower, while estimated uncertainties are still rather large ($\approx$ 30-50%). Lifetimes were found to be rather short (2.44$\pm$0.68 h) and show no distinct dependency on season or latitude, which might be a consequence of discarding observations at high solar zenith angles ($>65°$).

Main limitations of this (and similar) methods are the underlying assumptions of steady state (meaning constant emissions, wind fields and chemical conditions) within about 100 km downwind from a city, which is probably a too strong simplification in order to reach higher accuracies.

1   Introduction

Nitrogen oxides (NO_x=NO+NO_2) are important components of air pollution and play a key role in tropospheric chemistry. Satellite instruments such as the TROPOspheric Monitoring Instrument (TROPOMI) (Veefkind et al., 2012) measure various atmospheric constituents, among them NO_2. This allows investigation of e.g. various NO_x sources, their spatial distribution, or temporal patterns (Monks and Beirle, 2011, and references therein).

Satellite observations of NO_2 have been also used in the past to determine the emissions and lifetimes of NO_x from megacities. Using multi-annual observations from the Ozone Monitoring Instrument (OMI) (Levelt et al., 2006), Beirle et al. (2011) estimated lifetime and emissions for 8 megacities by (a) sorting and averaging the OMI observations separately for different wind directions and (b) fitting an exponentially modified Gaussian (EMG) distribution to the respective downwind patterns, yielding a first order time constant (effective lifetime) and emissions as fit parameters. Several studies applied a similar method in recent years (e.g., Valin et al., 2013; Pommier et al., 2013; de Foy et al., 2014; Lu et al., 2015; Liu et al., 2016; Lorente et al., 2019; Laughner and Cohen, 2019; Lange et al., 2022).

A modification widely used is the application of a "wind-rotation" technique, as proposed by Valin et al. (2013) and Pommier et al. (2013): The downwind patterns of individual overpasses are rotated according to wind direction before averaging. This yields one mean downwind pattern instead of e.g. 8 (for 8 wind directions as in Beirle et al. (2011)) and thus results in better
30   statistics.

A key assumption made in Beirle et al. (2011) and most follow-up studies is that the emissions are "point-source" like, i.e. can be described by a Gaussian function. However, this assumption is oftentimes not fulfilled, as there are often suburbs, neighbouring cities, power plants or industrial areas located in the surrounding of large cities. As shown in Liu et al. (2016), such interfering emission sources in the downwind plume lead to an overestimation of the lifetime (as the decay seems to be
35   slower), corresponding to an underestimation of emissions.

A different approach that works also for complex spatial distributions of multiple sources was proposed in Liu et al. (2016): Instead of assuming cities to represent a "point source", the observed pattern of NO_2 columns at calm wind conditions is used as proxy for the spatial distribution of emissions. From the comparison of the respective patterns for windy conditions, the effective NO_x lifetime can then be derived. As shown in Liu et al. (2016), the emissions of 53 cities and power plants in the
40   US and China could be derived, with very good agreement to bottom-up inventories (9% (mean) $\pm$ 49% (standard deviation)). Recently, the algorithm was refined further (Liu et al., 2022) such that lifetime and emissions are derived in a single step instead of the two step scheme in Liu et al. (2016). For this approach, however, the wind directions have to be considered separately, as the emission pattern is different for different directions. I.e., the wind rotation cannot be applied, so that longer time periods have to be averaged in order to reach sufficient statistics.

45   Still, there are some remaining issues:

1. The background level of NO_2 VCDs is included as one fit parameter in Liu et al. (2016) and Liu et al. (2022). However, the background itself depends on wind direction in many cases, and cannot generally be assumed to be the same for calm vs. windy conditions.

2. The method requires sufficient observations for calm conditions; otherwise, no proxy for the emission distribution is
50   available.

3. Even if only observations for calm conditions are considered, which still includes wind speeds up to 2 m s^{-1}, column density patterns are smeared out compared to real emission patterns, limiting the reachable agreement between observation and forward model.

In order to account for these aspects, a modified procedure was developed within ESA's "World Emission" project (World
55   Emission, 2022). The basic idea is to consider the spatial distribution of emissions also as fit parameters (compare Lorente et al., 2019); in order to have sufficient observations for a well constrained fit, the fit parameters (distribution of emissions, background and lifetime) are derived from the combined observations for calm conditions as well as two opposite wind directions.

2 Input Data

2.1 TROPOMI

60 The TROPOspheric Monitoring Instrument (TROPOMI) (Veefkind et al., 2012), operated by the European Space Agency (ESA), was launched onboard the Sentinel 5 Precursor (S5-P) mission in October 2017. It provides daily global measurements around 13:45 local time with ground pixel sizes down to 3.5×5.5 km^2.

The NO_x emission and lifetime estimates are based on TROPOMI NO_2 tropospheric vertical column densities (TVCDs) (van Geffen et al., 2019, 2022) for the period from May 2018 to November 2021, using the consistently reprocessed data
65 product provided via the S5-P Products Algorithm Laboratory (PAL) (Eskes et al., 2021) based on NO_2 processor version v2.3.1.

NO_2 is upscaled to NO_x based on a parameterization of the NO_2 photolysis rate as function of SZA (Dickerson et al., 1982), temperature fields from ERA5 (see next section), and modelled ozone concentrations, as described in detail in Beirle et al. (2023).

70 As in Beirle et al. (2023), we restrict the measurements to high quality data (qa values > 0.75), SZA<65° (which is the range recommended by Dickerson et al. (1982) for the photolysis parameterization), and VZA<56° (which eliminates the large TROPOMI ground pixel at the swath edges).

2.2 ERA5

Meteorological data is taken from ERA5 reanalysis (Hersbach et al., 2020) provided by the European Centre for Medium-
75 Range Weather Forecasts (ECMWF). Here, ERA5 data are used with a truncation at T639 of the Gaussian grid, corresponding to ≈0.3° resolution.

The ERA5 data is processed as in Beirle et al. (2023): "In order to reduce data amount, we created an intermediate meteorological dataset in which the original model output ... was interpolated on a regular horizontal grid with a resolution of 1° and stored in intervals of 6 hours." In the analysis below, these intermediate wind fields are interpolated in latitude/longitude and
80 time according to the TROPOMI measurements, and vertically to 500 m above ground level (agl).

2.3 World City Database

The emission/lifetime estimation algorithm is applied to all cities worldwide with more than one million citizens, yielding a list of initially 700 cities, based on the World Cities Database (WCD) as provided on simplemaps.com/data/world-cities.

2.4 EDGAR

85 The estimated emissions are compared to the Emissions Database for Global Atmospheric Research (EDGAR). Here we use gridded EDGAR NO_x emission data (0.1° grid), version 6.1, for the year 2018, https://edgar.jrc.ec.europa.eu/index.php/dataset_ap61. EDGAR NO_x emission data is provided on monthly basis for different emission sectors. We have compiled

3

monthly NO_x emissions by summing up all provided emission sectors, and seasonal NO_x emissions by averaging the respective months according to the season definition used in this study (see section 3.2).

3 Methods

3.1 Data sorting and gridding

As in Beirle et al. (2011), the satellite observations are averaged for different wind conditions (according to ERA5 wind fields 500 m agl). For this purpose, all TROPOMI observations are sorted into the wind sectors "calm" (i.e. wind speed w below 2 m s^{-1}) or 8 wind direction sectors with 45° steps (for $w \geq 2$ m s^{-1}). Figure 1 illustrates the definition of the wind sectors.
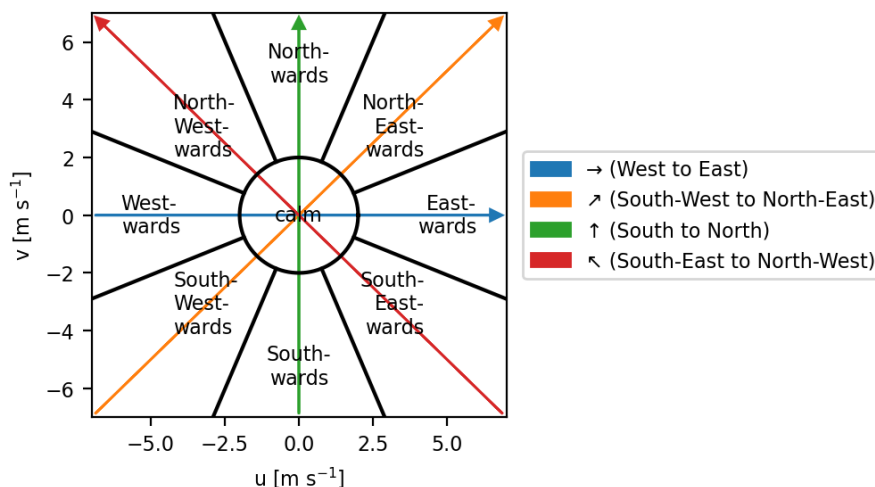

Figure 1. Definition of wind sectors (black) and wind axes (colored) based on wind speed (u, v). Note that "calm" is included in all 4 wind axes.

For each wind sector separately, the respective TROPOMI pixels are re-gridded on a regular lat-lon grid with 0.05° resolution.

3.2 Seasonal means

Emissions could potentially vary over the year. Likewise, the NO_x lifetime is expected to depend on season, in particular due to the impact of the SZA on photochemistry. Thus we perform the following analysis separately for different seasons.

As the NO_2 photolysis rate is driven by the SZA, which shows a seasonality with minimum and maximum close to the solstices, we define seasons accordingly as winter (NDJ: November, December, January), spring (FMA: February, March, April), summer (MJJ: May, June, July) and autumn (ASO: August, September, October) in this study. I.e. winter and summer comprise measurements of lowest and highest SZA, respectively, for the northern hemisphere.

For each wind sector and each season, the gridded NO_x column densities and the associated wind vectors are averaged separately. The seasonal mean NO_x column density for the different wind sectors is shown exemplarily for Riyadh in winter (Fig. 2) and Paris in summer (Fig. 3). The respective maps for all cities/seasons with successful fit (see below) are provided in the Supplement.

3.3 Considered distances

In this study, we consider two different distances for different purposes:

- For the investigation of the downwind patterns for different wind conditions, and the respective fit of the forward model (section 3.5), we consider distances of 145 km upwind/downwind.

- For the quantification of emissions, we consider distances of ± 50 km around the city center, which we consider large enough to actually cover the full extent of the city or conurbation, but small enough to limit interference with neighboring cities (which cannot always be avoided). This distance of 50 km is applied for the integration of columns to line densities in across-wind direction (section 3.4) as well as for the integration of the fitted emission density to total emissions (section 3.5). I.e. the derived emissions refer to a total area of 100×100 km^2.

3.4 Wind axes and line density sets

For each axis (West to East, South-West to North-East, South to North, and South-East to North-West; compare Fig. 1), the mean line density is calculated for calm conditions as well as forward and backward wind direction, by integrating the seasonal mean NO_x column density maps in across-wind direction ($\pm$ 50 km), yielding the NO_x amount per length unit. Line densities cover the range -145 km to 145 km on a 10 km grid, i.e. represent vectors of length 29. Note that the VCD for calm conditions is the same for each axis, but due to the integration in across-wind direction, the line densities for calm conditions are different for the 4 axes. The resulting line densities for Riyadh in winter and Paris in summer are displayed in Fig. 4. The respective line densities for all cities/seasons with successful fit (see below) are provided in the Supplement.
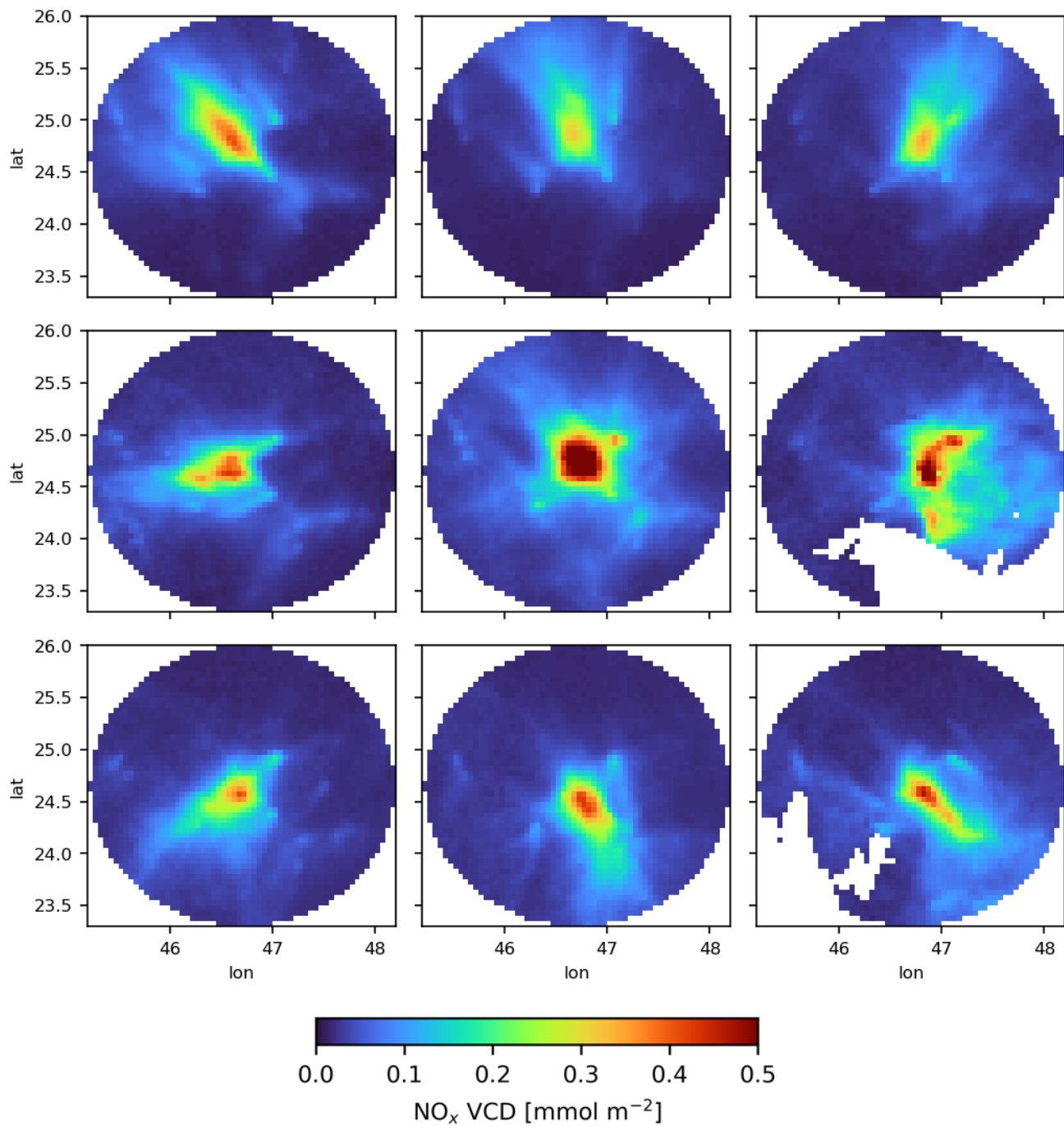
Figure 2. Mean NO_x distribution for Riyadh depending on wind conditions for winter months (NDJ) in the PAL period (May 2018-November 2021). The central panel displays the distribution for calm conditions ($w < 2$ m s^{-1}). The surrounding panels show the respective patterns for the 8 different wind sectors as defined in Fig. 1.
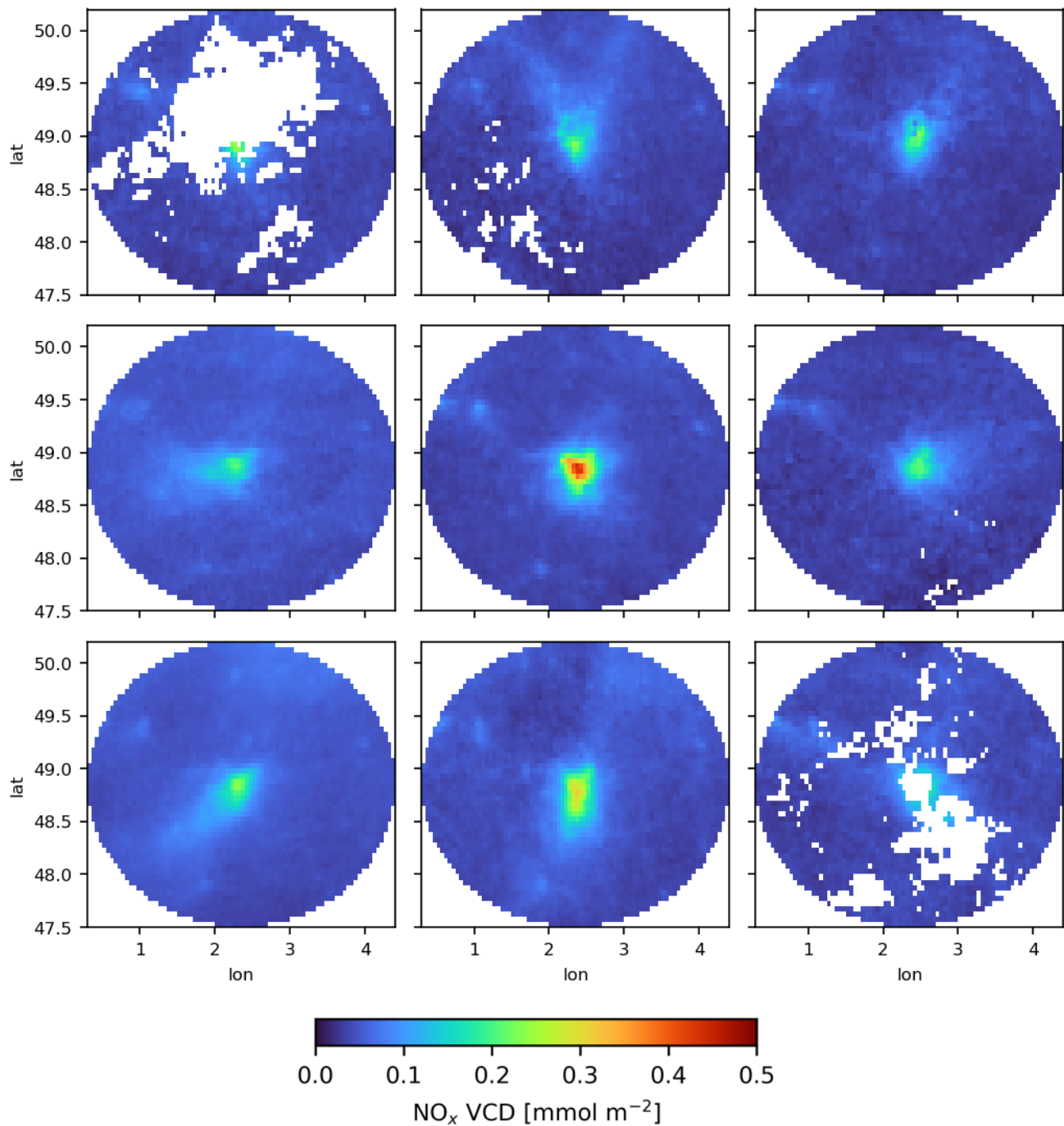
.

Figure 3. Mean NO_x distribution for Paris depending on wind conditions for summer months (MJJ) in the PAL period (May 2018-November 2021). The central panel displays the distribution for calm conditions ($w < 2$ m s^{-1}). The surrounding panels show the respective patterns for the 8 different wind sectors as defined in Fig. 1.
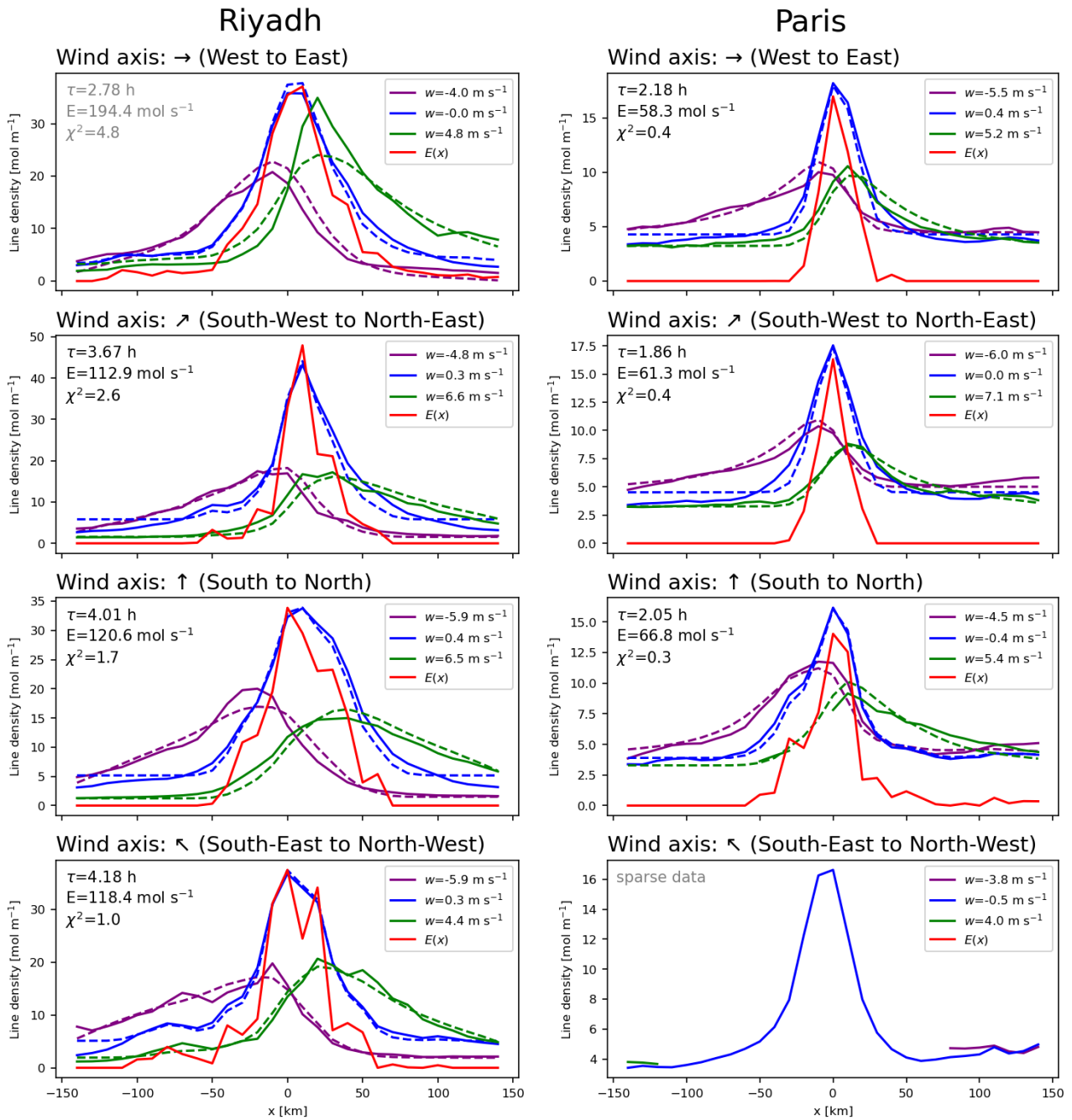
.

Figure 4. Mean NO_x line densities for (left) Riyadh in winter (NDJ) and (right) Paris in summer (MJJ) depending on wind conditions. The panels show the different wind axes. For each axis, the line densities for calm conditions (blue) and forward (green) and backward (purple) wind directions are displayed as straight lines. If the lifetime/emission fit succeeds, the corresponding fitted line densities are shown as dashed lines, and the fitted emission density is displayed in red. Fitted lifetime and emissions are provided as text in each panel, whereby grey indicates poor fit results which are discarded (see section 3.6).

3.5 Lifetime and emission fit

The lifetime and emission estimates are determined from a non-linear least squares inversion ("fit") that uses the observed patterns of line densities for calm conditions as well as forward and backward winds simultaneously.

The fit is performed for each axis (compare Fig. 1) separately based on the following forward model:

$$L_i(x) = E(x) * \exp\left(\frac{-x}{w_i \cdot \tau}\right) * \exp\left(\frac{-x^2}{2\sigma^2}\right) + b_i \tag{1}$$

The index i refers to the three different wind conditions (calm, forward, backward). $L_i(x)$ denotes the line densities, i.e. the columns integrated in across-wind direction, for calm, forward, and backward wind conditions. $E(x)$ represents the spatial density of emissions. It is considered to be the same for all 3 wind conditions. The symbol "*" indicates mathematical convolution. The first convolution term (to be truncated to $x > 0$) describes the downwind decay of the emitted NO_x with the e-folding lifetime τ, which is converted to an e-folding distance by multiplication with the mean wind speed w_i. The second convolution represents a simple Gaussian smoothing that accounts for effects like e.g. the temporal variation of wind speeds as well as the extent of the TROPOMI ground pixels. σ is fixed to 7 km; different a-priori values for σ hardly modify the results. b_i is the respective (wind dependent) NO_x background line density.

Based on the observed line densities within 145 km of the city center, the distribution of emission densities $E(x)$, lifetime τ and backgrounds b_i are fitted simultaneously. I.e. the free parameters (29 components of E, 3 components of b, and τ, in total 33 parameters) are constrained by up to $3 \times 29 = 87$ components of the measured line densities L_i.

Figure 4 displays the measured (straight) and fitted (dashed) line densities for Riyadh in winter and Paris in summer, respectively. The fitted emission densities $E(x)$ are shown in red. Note that $E(x)$ has the same unit as $L(x)$ (amount per length unit) and corresponds to the hypothetical line density in case of no wind transport, no background and no smoothing. For real observations, $E(x)$ (red line) is similar to $L(x)_{calm}$ (blue line), but not identical due to the effects of smoothing, background, and "calm" considering wind speeds not being zero, but < 2 m s^{-1}.

The emission rate of the considered hot spot is then derived by spatial integration of $E(x)$ from -50 km to +50 km (yielding the total amount of NO_x), divided by τ (yielding emission rates in amount per time unit). Likewise, $E(x)$ is integrated for $x < -50$ km and $x > 50$ km in order to check for and flag potential interfering sources (see next section).

The respective fit results for all cities and seasons with successful fit are included in the line density plots provided in the Supplement.

3.6 Selection and averaging of fit results

The forward model described above allows to quantify the emission distribution and total emissions around large cities. However, for robust fit results, a sufficient number of observations is necessary. Thus, a fit is only performed if

- at least 2 wind conditions have sufficient data (less then 10% spatial gaps in the seasonal mean column density map), and

- the difference in wind speed is sufficiently large (4 m s^{-1} between calm and windy conditions (forward or backward), or 8 m s^{-1} between for- and backward wind) in order to constrain the fit procedure by clearly distinct outflow patterns.

From the 11200 combinations (700 cities, 4 seasons, 4 axes), a fit was performed for 2154 cases. These fit results are considered further only if

- the reduced χ^2 of the fit is < 3. This is fulfilled for 1862 cases, i.e. in 86% of all performed fits. This criterion removes fit results of poor performance. For instance, for Riyadh in summer, the observed eastward outflow for westerly winds is not as pronounced as for the other wind directions (Fig. 2), and the respective line densities are not reproduced well by the forward model (green line for the first wind axis for Riyadh in Fig. 4). Due to the enhanced χ^2 of 4.8, this wind axis is skipped. The reason for the poor match of the fitted line densities is probably that ERA5 wind speeds and/or directions are not matching well to the actual transport for the observations sorted into the West-to-East direction.

- the fitted lifetime is plausible, i.e. between 1 and 10 hours. This selection skips 151 fits with too low lifetime, and 34 fits with too long lifetime.

- interfering emissions (i.e. $E(x)$ integrated for $x < $ -50 km or $x > $ 50 km) are lower than the city emissions themselves. In case of interfering emissions, the city is completely removed from the further analysis.

Finally, for each city, the results for the different axes are averaged, weighted by the number of contributing wind conditions for each axis (the more observations, the higher the weight) as well as the fit performance (the lower the χ^2, the higher the weight). Minimum requirement is that the fit worked for at least one season with either one axis where fit results for all 3 wind conditions are available, or two or more axes where fit results for 2 wind conditions are available.

With these strict selection criteria, emissions were derived for 100 cities out of the original list of 700 cities with > 1 million inhabitants. Note that for most cities, valid emission estimates could only be derived for 1 or 2 seasons; in total, 210 lifetime/emission estimates could be made.

4 Results

Within this study, seasonal mean NO$_x$ lifetimes and emissions were derived for 100 cities. The results are listed in Table 1. Below we analyze the results for emissions and lifetimes in more detail.

4.1 Emissions

Figure 5 displays a comparison of the derived seasonal emissions compared to EDGAR (v6.1, integrated over an area of 100×100 km^2 corresponding to the ranges of ± 50 km applied for across-wind integration of VCDs as well as for the integration of emission densities). Overall, the comparison is reasonable; the emissions from both data sources show a correlation of R=0.72. On average, the ratio TROPOMI/EDGAR is 1.05 (mean of individual ratios) and 0.86 (ratio of means), respectively.

Table 1. Seasonal NO_x emissions and lifetimes for 100 megacities. Seasons are defined as spring (FMA), summer (MJJ), autumn (ASO), and winter (NDJ); for cities in the Southern hemisphere, the actual meteorological season is flipped.

#	City	Lat [°N]	Lon [°E]	Emissions [kg s^{-1}]				Lifetimes [h]			
				Spring	Summer	Autumn	Winter	Spring	Summer	Autumn	Winter
1	Delhi	28.67	77.22		2.45				1.83		
2	Seoul	37.56	126.99		9.85				1.79		
3	Cairo	30.04	31.24	6.74	4.45			3.08	2.41		
4	New York	40.69	-73.92		4.25	3.60			2.37	3.14	
5	Moscow	55.76	37.62		7.79				2.53		
6	Buenos Aires	-34.60	-58.38	3.51		4.68	4.25	2.67		3.21	1.71
7	Istanbul	41.01	28.96	4.03	2.18	2.60		3.99	2.74	3.82	
8	Karachi	24.86	67.01	2.73		2.39		3.01		2.97	
9	Rio de Janeiro	-22.91	-43.20		4.24				1.54		
10	London	51.51	-0.13		2.72				3.80		
11	Paris	48.86	2.35		2.69	3.43			2.03	2.09	
12	Zhengzhou	34.75	113.66	7.38		4.29		2.25		2.99	
13	Wuhan	30.59	114.29		3.63	5.07			2.04	2.27	
14	Chicago	41.84	-87.69		2.52	2.70			3.05	3.33	
15	Changsha	28.20	112.97	2.94		2.42		2.33		1.57	
16	Nanning	22.82	108.31			3.53				1.14	
17	Shenyang	41.80	123.43		6.02	6.40			2.33	2.75	
18	Riyadh	24.65	46.71	4.87	6.14	6.44	5.19	3.35	3.22	3.61	4.03
19	Miami	25.78	-80.21				1.49				3.21
20	Baghdad	33.35	44.42	6.22	5.02	5.02	6.89	1.77	2.38	2.83	3.13
21	Khartoum	15.60	32.53		0.88	1.04			2.06	1.85	
22	Madrid	40.42	-3.72	5.38	2.00	2.99		1.65	1.94	1.84	
23	Dallas	32.79	-96.77	1.88	1.40	1.37		4.19	2.23	2.83	
24	Giza	29.99	31.21	5.91	4.25			3.48	2.52		
25	Houston	29.79	-95.39		2.39	2.23	3.41		1.94	2.43	3.89
26	Atlanta	33.76	-84.42	1.92	1.44	1.12	2.20	3.53	1.73	2.65	4.25
27	Toronto	43.74	-79.37		1.99	1.87			2.44	2.65	
28	Xiaoganzhan	30.93	113.91		1.42	2.39			2.68	2.30	
29	Boston	42.32	-71.08		1.66	0.88			1.79	3.92	
30	Harbin	45.75	126.63		2.21	2.68			2.83	3.19	
31	Melbourne	-37.81	144.96				3.27				1.99
32	Zibo	36.78	118.05		3.01	3.22			2.45	3.60	
33	Casablanca	33.60	-7.62	2.42			2.52	1.82			2.17
34	Phoenix	33.57	-112.09	3.21			3.35	1.62			1.61
35	Liuzhou	24.33	109.43			1.96	2.33			1.42	2.60
36	Jeddah	21.54	39.17		2.53				2.11		
37	Kano	12.00	8.52	0.71		0.49		3.80		1.87	
38	Berlin	52.52	13.38		0.65				2.35		
39	Montréal	45.51	-73.56			1.51				2.81	
40	Detroit	42.38	-83.10		1.59	1.69			1.97	2.65	
41	Algiers	36.78	3.06	4.76	3.11	3.97	6.74	2.12	1.44	1.51	1.88
42	Kuwait City	29.38	47.98	5.48	4.13	5.02	5.35	3.01	3.35	2.98	3.41
43	Minneapolis	44.96	-93.27		1.17	1.39			2.57	2.84	
44	Kyiv	50.45	30.52		1.03	1.39			2.07	3.16	
45	Incheon	37.46	126.65		10.16				1.79		
46	Baotou	40.66	109.83	5.48	6.00	7.59		3.00	1.40	1.76	
47	Brooklyn	40.65	-73.95		3.92	3.59			2.43	3.20	
48	Dubai	25.27	55.31	6.75	6.68			2.79	1.90		
49	Omdurman	15.62	32.48		1.02	1.10			1.99	1.82	
50	Ghāziābād	28.67	77.42		2.69	2.25			1.77	3.18	

Table 1. (continued)

| #	City	Lat [°N]	Lon [°E]	Emissions [kg s^{-1}]				Lifetimes [h]			
				Spring	Summer	Autumn	Winter	Spring	Summer	Autumn	Winter
51	Queens	40.75	-73.80		3.83	3.57			2.61	3.04	
52	Baku	40.37	49.84		1.11	1.23			1.92	2.32	
53	Havana	23.14	-82.36			0.41				2.82	
54	Las Vegas	36.23	-115.27	1.64	0.76	1.16	3.30	1.54	1.91	1.70	1.34
55	Vadodara	22.30	73.20	1.32				2.41			
56	San Antonio	29.47	-98.53			0.97	1.53			2.26	3.16
57	Perth	-31.95	115.86	1.10	1.55	1.29		1.91	2.16	1.86	
58	Vishākhapatnam	17.73	83.32			0.81				3.08	
59	St. Louis	38.64	-90.25		1.13	1.06			1.86	2.45	
60	Minsk	53.90	27.56		0.59	0.89			2.08	2.93	
61	Vienna	48.21	16.37		1.20	0.95			1.29	2.24	
62	Bucharest	44.40	26.08		0.75	0.92			1.81	2.57	
63	Liaoyang	41.26	123.18		6.89	5.92			2.08	3.33	
64	Warsaw	52.23	21.01			0.90				3.39	
65	Budapest	47.50	19.04	1.62	0.82	1.53		2.94	1.82	1.86	
66	Pittsburgh	40.44	-79.98		1.50	1.09			1.50	2.23	
67	Cincinnati	39.14	-84.51		0.67	0.80			2.06	3.50	
68	Kansas City	39.12	-94.55	1.03	0.52	0.73		3.30	2.19	2.41	
69	Manhattan	40.78	-73.97		3.72	3.77			2.38	2.99	
70	Novosibirsk	55.03	82.92		1.12				3.60		
71	Charlotte	35.21	-80.83	0.69		0.80	1.80	4.20		2.44	2.52
72	Porto Alegre	-30.03	-51.23	0.79	2.14	1.54	1.06	2.05	1.86	1.97	1.91
73	Bronx	40.85	-73.87		3.67	3.72			2.67	2.86	
74	Farīdābād	28.44	77.31		2.59				1.96		
75	Ulaanbaatar	47.92	106.91		0.43	0.89			3.27	2.87	
76	Belgrade	44.82	20.47	2.11	1.42	1.53		2.33	1.61	2.36	
77	Córdoba	-31.42	-64.18		0.63	0.51	0.45		2.95	2.75	1.36
78	Juárez	31.74	-106.49		1.18	1.25	2.34		1.75	1.97	2.19
79	Adelaide	-34.93	138.60	1.19		1.34	1.08	2.28		2.17	1.88
80	Nizhniy Novgorod	56.33	44.01		0.98				1.79		
81	Sharjah	25.36	55.39	5.94	6.64		8.39	3.20	1.85		2.36
82	Kazan	55.79	49.11		0.94	0.94			1.85	2.76	
83	Suwon	37.29	127.01		10.73				1.81		
84	Chelyabinsk	55.15	61.40		1.35	2.27			2.92	2.99	
85	Omsk	54.97	73.38		0.85				3.31		
86	Ulsan	35.55	129.32		3.55	4.93			1.91	1.57	
87	Tripoli	32.88	13.19	2.44	2.21	2.16	2.89	1.87	1.67	1.94	1.87
88	Rostov	47.23	39.72		0.90	1.68			3.13	2.65	
89	Ufa	54.73	55.95		0.82	1.11			2.09	2.68	
90	Xibeijie	39.74	98.50		0.99	0.98			2.02	2.52	
91	Copenhagen	55.68	12.56		0.51	0.41			3.53	4.54	
92	Hanchuan	30.65	113.83		2.69	3.66			2.12	2.16	
93	Krasnoyarsk	56.01	92.87		1.05	1.37			1.77	1.52	
94	São Gonçalo	-22.83	-43.05		4.54				1.53		
95	Nashville	36.17	-86.78	1.07	0.57	0.81	1.74	2.12	1.69	2.17	2.18
96	Goyang	37.66	126.83		9.42				1.78		
97	Edmonton	53.53	-113.49		1.75				2.32		
98	Tunis	36.80	10.18	1.67	1.05	1.37		2.71	2.17	2.39	
99	Shubrā al Khaymah	30.13	31.24	6.94	4.67			2.90	2.39		
100	Volgograd	48.71	44.51		0.69	0.72			1.93	3.30	
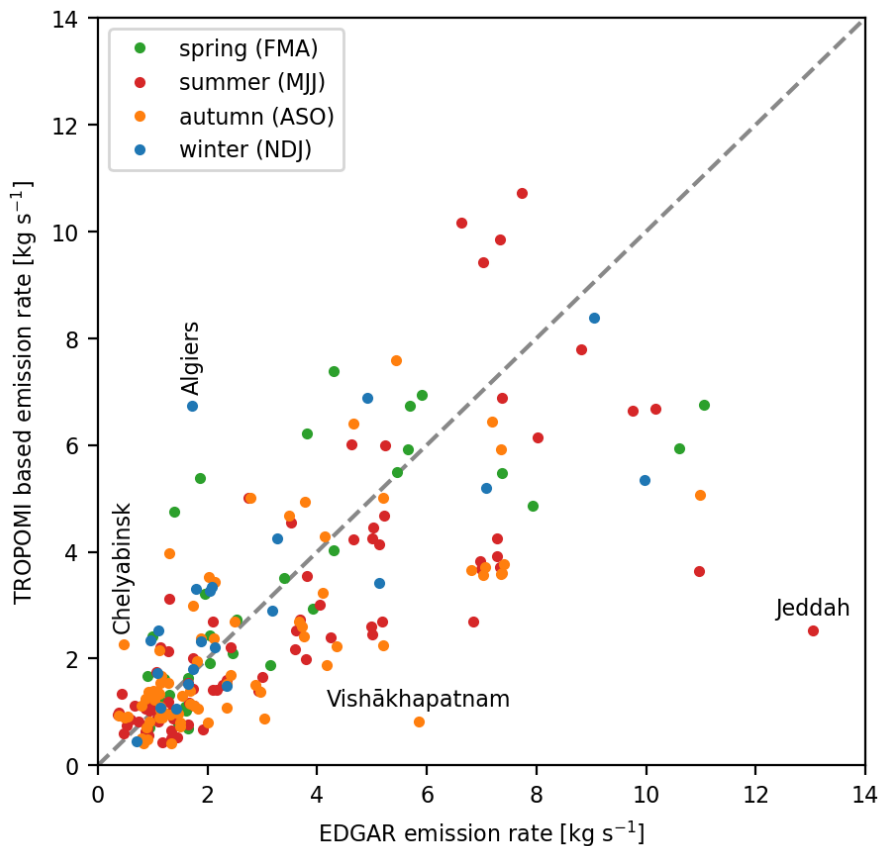
Figure 5. Seasonal NO_x emissions from TROPOMI, averaged over the PAL period May 2018 to November 2021 (y-axis), as compared to the respective EDGAR emissions for 2018 (x-axis), integrated over an area of 100×100 km^2. Uncertainties for the TROPOMI-based estimates are about 30-50% (section 5.2). City labels indicate cases with highest and lowest ratios, respectively, which are discussed in more detail in section 5.3.

185 However, fluctuations are quite large. The most extreme deviations (labeled by city name in Fig. 5) are discussed in detail in section 5.3.

A combined seasonal analysis (like the mean seasonality of all cities, or cities within a latitude range) is not meaningful as there are seasons missing for most cities. Thus we focus on those 9 cities where the fit worked for all seasons (Fig. 6). The resulting seasonal cycles differ with respect to amplitude and patterns: while there is low seasonal variety found for Tripoli,

190 emissions are maximal in summer and autumn for Riyadh, but minimal for Baghdad. Also the comparison to EDGAR is rather diverse: patterns are very similar for Baghdad, but different for e.g. Riyadh. For some cities, EDGAR does not show seasonality, but TROPOMI does (Algiers, Las Vegas, Porto Alegre), while for others, the opposite is the case (Kuwait city, Tripoli).

13
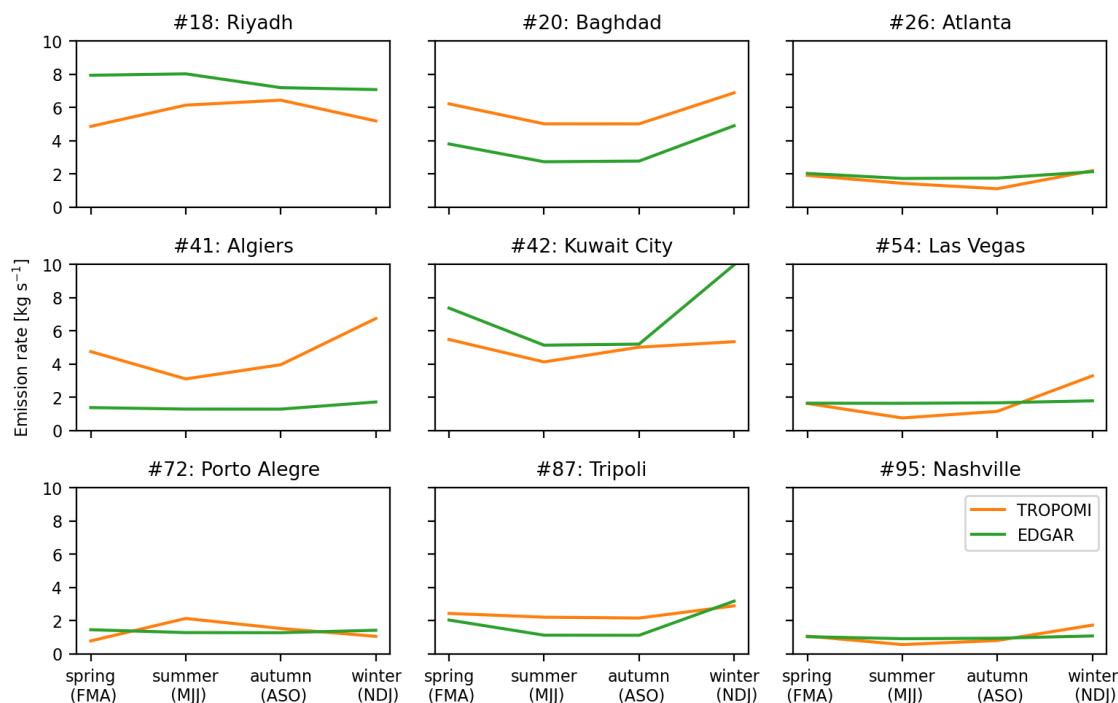
Figure 6. Seasonality of emissions based on TROPOMI estimates (orange) and according to EDGAR (green) for those 9 cities where the retrieval yields results for all seasons.

4.2 Lifetimes

The lifetime fit based on Eq. 1 generally yields stable fit results for τ for individual wind axes. Few remaining outliers (below
195 1 h or above 10 h) have been removed by the selection criteria described in section 3.6.

The resulting weighted mean lifetimes for the considered cities are generally quite short (2.44 hours on average) and show only low variability (0.68 hours standard deviation). Figure 7 displays (a) a histogram of the fitted lifetimes, and (b) the seasonal results (color coded) as function of latitude. The latter do not reveal a clear pattern of higher lifetimes at higher latitudes or in hemispheric winter (see section 5.4).

200 ## 5 Discussion

5.1 Benefits

Satellite measurements of the downwind plume evolution of urban emissions yield model independent, observation-based constraints of the cities emissions and the corresponding effective lifetime. Compared to previous studies, the proposed new method of fitting the downwind patterns of opposing wind directions at the same time has several advantages:
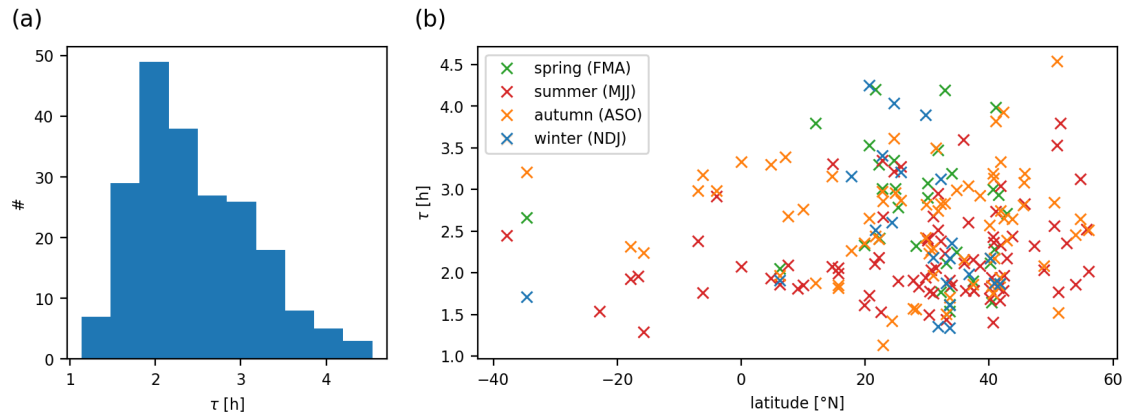
Figure 7. Derived effective lifetimes τ. (a) Histogram of seasonal lifetime results for the 100 investigated cities. (b) Latitudinal dependency of seasonal (color coded) lifetimes. Seasons are defined as winter (NDJ), spring (FMA), summer (MJJ) and autumn (ASO); for cities in the Southern hemisphere, the actual meteorological season is flipped.

1. Instead of assuming the emissions to be distributed by a Gaussian, possible spatial variations of emissions are explicitly considered.

2. A potential wind dependency of the background is accounted for.

3. The fit is generally well constrained by the spatial patterns for opposite wind directions, resulting in realistic lifetime fits in most cases.

5.2 Errors and limitations

5.2.1 NO$_2$ columns

For v1 of the TROPOMI NO$_2$ column densities, a low-bias was reported over urban areas (Judd et al., 2020; Lange et al., 2023). In the PAL dataset, based on the NO$_2$ processor version v2.3.1, many retrieval steps have been improved. In particular an improved cloud algorithm has been used, resulting in higher cloud altitudes, thus lower air-mass factors and higher NO$_2$ columns (Eskes et al., 2021; van Geffen et al., 2022). Thus, the reported low-bias is expected to be reduced. However, any remaining bias in the NO$_2$ column would directly affect the presented (as well as any other TROPOMI-based) emission estimate.

5.2.2 Wind fields

In this study, we use ERA5 wind fields, which have been stored on a 1° grid and 6 hour intervals in order to reduce data amount, at the cost of wind field accuracy. We are currently preparing the implementation of high-resolution ERA5 wind data with hourly sampling on 0.25° latitude/longitude grid for future studies. So far, we applied high-resolution wind data for the calculation of the advection of SO$_2$ fluxes (Adrian Jost et al., in preparation) based on the algorithm developed for

NO_x (Beirle et al., 2023). On average, emission estimates for high resolution wind fields were found to be higher by about 5%. Such a systematic effect is expected, since any error in wind direction $\Delta\alpha$, random or systematic, causes a underestimation of the wind component in the actual wind direction, thus an overestimation of lifetimes, and an underestimation of emissions (see Supplement of Beirle et al. (2019)).

But even with high-resolution wind fields, the simplified description of horizontal transport of the whole tropospheric column by one horizontal wind field (here: interpolated at 500 m agl) remains a significant source of uncertainty for this and similar methods. As discussed in Beirle et al. (2011), uncertainties of emissions due to uncertainties in wind fields are about up to 30%.

5.2.3 Lifetime & emission fit

Within the non-linear least squares optimization applied to Eq. 1, the best matching parameters are determined, including their uncertainties. As the new approach of applying patterns for forward, backward, and calm wind conditions simultaneously is strongly constrained, results are generally robust, and the nominal uncertainties resulting from the least squares inversion are generally low (down to few percent) and negligible compared to other uncertainties. Thus, the fit errors are not listed.

More realistic uncertainties could in principle be estimated from the standard deviation of fit results among different wind axes. For the example of Riyadh shown in Fig. 4, this would yield 24% uncertainty for emission rates, and 15% for lifetimes. Note, however, that the "outlier" for wind axis "$\longrightarrow$" is not considered in the reported mean emissions for Riyadh due to the high χ^2 value. As there are often only one or two axes available for most cities, this procedure cannot be used for calculating a standard deviation for all cities. But since observation conditions are close to optimal for Riyadh (high albedo, few clouds), higher uncertainties have to be expected for other cities.

One reason for this rather large uncertainty of the fit results – despite the strong constraint from downwind patterns in opposite directions – is probably the assumption of steady state (over distances up to 145 km downwind), while in reality, emissions, wind fields and chemistry are changing over time.

Overall, we roughly estimate the total uncertainty (including wind) of the estimated emissions to typically 30% up to 50%.

5.3 Emissions

There are some aspects that have to be kept in mind when interpreting the derived emissions and the comparison to EDGAR:

– Given emission rates are meant to represent the integrated emissions within $\pm$ 50 km from city center in both directions, corresponding to the chosen across-wind range used for calculating line densities and the integration range of the fitted emission density $E(x)$.

This implies that the emissions from large cities close to each other interfere and are counted for each city repeatedly (for the TROPOMI estimate as well as for the estimated EDGAR value). This happens for instance for the large cities around Seoul, i.e. Incheon, Suwon and Goyang, which are all listed with emission rates close to 10 kg s^{-1}. These values must not be added.

255   – EDGAR emissions are provided for the year 2018, while the TROPOMI estimate is derived for the time range covered
        by PAL (May 2018 – November 2021), thus deviations have to be expected in case of recent changes in emissions. This
        is particularly the case for the massive lockdowns in 2020 and 2021.

For these reasons, and due to the estimated uncertainty of up to 50% (see section 5.2), no perfect agreement can be expected.
Actually, for most cities and seasons, the TROPOMI based estimates agree with EDGAR within the given uncertainties.
260 However, for some cities, large deviations have been observed which exceed the estimated uncertainty by far:

        – TROPOMI-based emissions for Algiers (#41) in winter and Chelyabinsk (#84) in autumn are higher than EDGAR
        emissions by a factor of 3.9 and 4.9, respectively. Figure 8 displays the spatial distribution of NO_x emissions according to
        EDGAR around these cities, as compared to the observed NO_x pattern for calm wind conditions. In both cases, EDGAR
        emissions within the city are very low, but additional sources show up in the EDGAR emissions west of Algiers (Hadjret
265   en Nouss power plant) and South of Chelyabinsk (Yuzhnouralskaya and Troitskaya power plants). The TROPOMI VCD,
        however, does not show indications for strong point sources at these locations. [1] For Algiers, emission estimates were
        derived for all seasons (Fig. 6), with winter emissions found to be more than twice than summer emissions. In contrast,
        EDGAR emissions hardly show any seasonality. But for all seasons, TROPOMI based estimates are significantly higher
        than EDGAR.

270   – For Jeddah (#36) in summer and Vishākhapatnam (#58) in autumn, EDGAR emissions are higher than the TROPOMI
        based estimate by a factor of 5.2 and 7.2, respectively. Mean TROPOMI NO_x VCDs are far lower than would be expected
        for the given EDGAR emissions (Fig. 9).

    For all of these cities, the lifetime and emission fits work properly (see Supplement), and the fitted lifetimes are well within
the typical range found for other cities (Table 1). Thus we conclude that our comparison actually hints to too low/too high
275 EDGAR emissions which should be checked for these cities.

5.4 Lifetimes

The effective NO_x lifetime has been found to be rather short (few hours, 2.44 h on average) with only weak variability (0.68 h
SD). These values are generally consistent with low NO_x lifetimes reported in previous studies (de Foy et al., 2014; Laughner
and Cohen, 2019; Lorente et al., 2019; Laughner and Cohen, 2019; Lange et al., 2022).
280   In contrast to Lange et al. (2022), however, we do not find a clear increase of lifetime with latitude or a clear seasonal
dependency. This should be investigated further, but is probably - at least partly - related to the strict SZA<65° criterion
applied in this study, resulting in the removal of wintertime measurements at mid- and high latitudes. Thus, larger lifetimes in
winter would be probably observed with this method as well if larger SZA would be included.

---

[1]Yuzhnouralskaya was actually identified in the point source catalog (Beirle et al., 2023), but estimated emissions (0.13 kg s^{-1}) are one order of magnitude lower than that listed in EDGAR (1.2 kg s^{-1} in autumn).
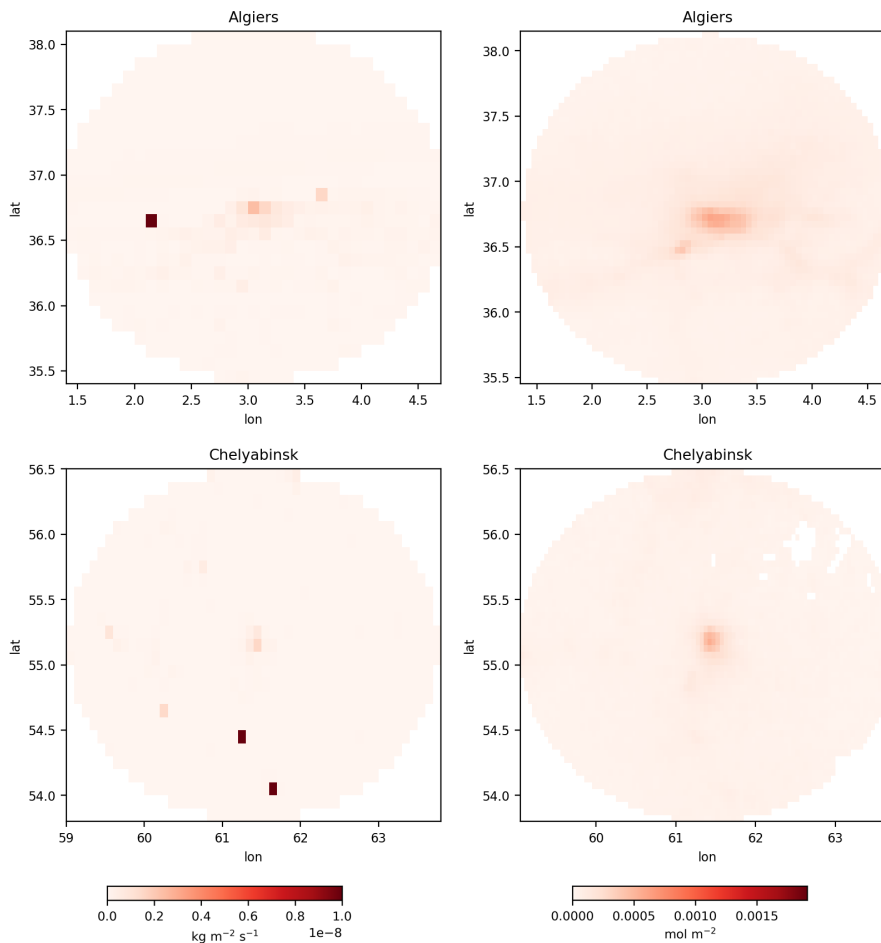
Figure 8. EDGAR NO_x emissions (left) and TROPOMI NO_x VCDs for calm wind conditions (right) around Algiers (#41) in winter (top) and Chelyabinsk (#84) in autumn (bottom). The colorbar for VCDs corresponds to the emission colorbar for mass conservation with a lifetime of 2.44 h.

6 Conclusions

285   We present a new method for the estimation of urban emissions of NO_x and the corresponding effective lifetime of NO_x. Compared to previous methods of fitting an EMG to the downwind plume (intrinsically assuming a "point source"), we invert the downwind patterns of opposing wind directions simultaneously. This approach has two major advantages: 1. the spatial distribution of emission sources within a city can be resolved, and 2. the fit is generally well constrained. The main disadvantage is that the method requires temporal mean patterns for opposing wind directions and thus only works on long-term temporal

290   averages.
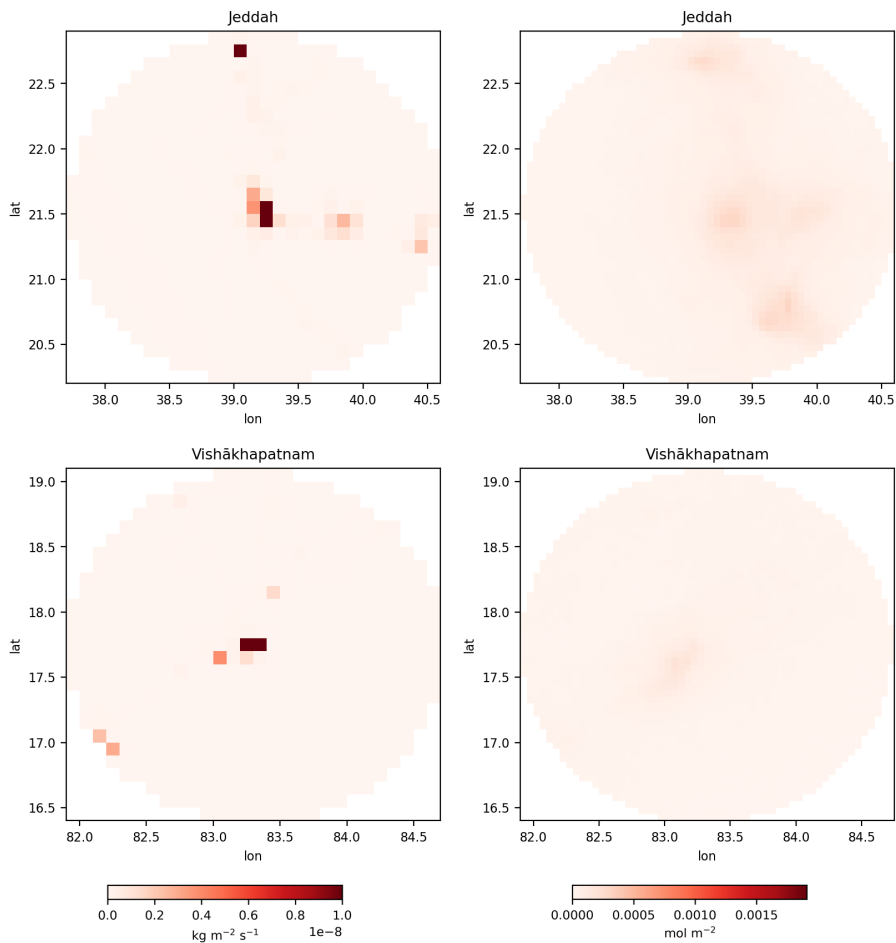
Figure 9. EDGAR NO_x emissions (left) and TROPOMI NO_x VCDs for calm wind conditions (right) around Jeddah (#36) in summer (top) and Vishākhapatnam (#58) in autumn (bottom). The colorbar for VCDs corresponds to the emission colorbar for mass conservation with a lifetime of 2.44 h.

Within ESA's World Emission project, the method was successfully applied to 100 cities worldwide. The derived emissions show reasonable agreement to EDGAR emissions (R=0.72, ratio of means 0.86). The cities with largest deviations have been checked in more detail and could be explained by a spatial mismatch or a high bias of EDGAR emissions.

Lifetimes were found to be 2.44 ± 0.68 hours on average. No clear seasonal or latitudinal dependency was found, but this might be due to the removal of observations with large SZA (>65°).

The remaining uncertainties and the partly inconsistent results for different wind axes have to be considered in relation to the assumptions made:

– the assumption of steady state (within 145 km downwind of the city center),

– the representation of the complex and nonlinear NO_x chemistry by one single first order loss time constant,

19

300 – the simplified representation of transport by horizontal wind fields, ignoring 3d effects and different wind fields at different altitudes of the column.

These assumptions cause intrinsic uncertainties of the presented (as well as other similar) methods, which probably cannot simply be removed just by improved algorithms.

References

Beirle, S., Boersma, K. F., Platt, U., Lawrence, M. G. and Wagner, T.: Megacity Emissions and Lifetimes of Nitrogen Oxides Probed from Space, Science, 333(6050), 1737–1739, doi:10.1126/science.1207824, 2011.

Beirle, S., Borger, C., Dörner, S., Li, A., Hu, Z., Liu, F., Wang, Y., and Wagner, T.: Pinpointing nitrogen oxide emissions from space, Sci. Adv. 5, doi:https://doi.org/10.1126/sciadv.aax9800, 2019.

Beirle, S., Borger, C., Jost, A., and Wagner, T.: Catalog of NO_x point source emissions (version 2), World Data Center for Climate (WDCC) at DKRZ, https://doi.org/10.26050/WDCC/No_xPointEmissionsV2, 2023.

de Foy, B., Wilkins, J. L., Lu, Z., Streets, D. G., and Duncan, B. N.: Model evaluation of methods for estimating surface emissions and chemical lifetimes from satellite data, Atmos. Environ., 98, 66–77, 2014.

Dickerson, R. R., Stedman, D. H., and Delany, A. C.: Direct Measurements of ozone and Nitrogen Dioxide Photolysis Rates in the Troposphere, J. Geophys. Res., 87, 4933–4946, https://doi.org/10.1029/JC087iC07p04933, 1982.

Eskes, H., van Geffen, J., Sneep, M., Veefkind, P., Niemeijer, S., and Zehner, C.: S5P Nitrogen Dioxide v02.03.01 intermediate reprocessing on the S5P-PAL system: Readme file, [online] Available from: https://www.temis.nl/airpollution/no2col/docs/S5P-KNMI-PRF-PAL_reprocessing_NO2_v02.03.01_20211215.pdf, 2021.

Hersbach, H., Bell, B., Berrisford, P., Hirahara, S., Horányi, A., Muñoz-Sabater, J., Nicolas, J., Peubey, C., Radu, R., Schepers, D., Simmons, A., Soci, C., Abdalla, S., Abellan, X., Balsamo, G., Bechtold, P., Biavati, G., Bidlot, J., Bonavita, M., Chiara, G. D., Dahlgren, P., Dee, D., Diamantakis, M., Dragani, R., Flemming, J., Forbes, R., Fuentes, M., Geer, A., Haimberger, L., Healy, S., Hogan, R. J., Hólm, E., Janisková, M., Keeley, S., Laloyaux, P., Lopez, P., Lupu, C., Radnoti, G., Rosnay, P. de, Rozum, I., Vamborg, F., Villaume, S., and Thépaut, J.-N.: The ERA5 global reanalysis, Quarterly Journal of the Royal Meteorological Society, 146, 1999–2049, https://doi.org/10.1002/qj.3803, 2020.

Judd, L. M., Al-Saadi, J. A., Szykman, J. J., Valin, L. C., Janz, S. J., Kowalewski, M. G., Eskes, H. J., Veefkind, J. P., Cede, A., Mueller, M., Gebetsberger, M., Swap, R., Pierce, R. B., Nowlan, C. R., Abad, G. G., Nehrir, A., and Williams, D.: Evaluating Sentinel-5P TROPOMI tropospheric NO2 column densities with airborne and Pandora spectrometers near New York City and Long Island Sound, Atmos. Meas. Tech., 13, 6113–6140, https://doi.org/10.5194/amt-13-6113-2020, 2020.

Lange, K., Richter, A., and Burrows, J. P.: Variability of nitrogen oxide emission fluxes and lifetimes estimated from Sentinel-5P TROPOMI observations, Atmos. Chem. Phys., 22, 2745–2767, https://doi.org/10.5194/acp-22-2745-2022, 2022.

Lange, K., Richter, A., Schönhardt, A., Meier, A. C., Bösch, T., Seyler, A., Krause, K., Behrens, L. K., Wittrock, F., Merlaud, A., Tack, F., Fayt, C., Friedrich, M. M., Dimitropoulou, E., Van Roozendael, M., Kumar, V., Donner, S., Dörner, S., Lauster, B., Razi, M., Borger, C., Uhlmannsiek, K., Wagner, T., Ruhtz, T., Eskes, H., Bohn, B., Santana Diaz, D., Abuhassan, N., Schüttemeyer, D., and Burrows, J. P.: Validation of Sentinel-5P TROPOMI tropospheric NO2 products by comparison with NO2 measurements from airborne imaging DOAS, ground-based stationary DOAS, and mobile car DOAS measurements during the S5P-VAL-DE-Ruhr campaign, Atmos. Meas. Tech., 16, 1357–1389, https://doi.org/10.5194/amt-16-1357-2023, 2023.

Laughner, J. L. and Cohen, R. C.: Direct observation of changing NO_x lifetime in North American cities, Science, 366, 723–727, https://doi.org/10.1126/science.aax6832, 2019.

Levelt, P. F., van den Oord, G. H. J., Dobber, M. R., Mälkki, A., Visser, H., de Vries, J., Stammes, P., Lundell, J., and Saari, H.: The Ozone Monitoring Instrument, IEEE T. Geosci. Remote, 44, 1093–1101, https://doi.org/10.1109/TGRS.2006.872333, 2006a.

Liu, F., Beirle, S., Zhang, Q., Dörner, S., He, K., and Wagner, T.: NO_x lifetimes and emissions of cities and power plants in polluted
350   background estimated by satellite observations, Atmos. Chem. Phys., 16, 5283–5298, https://doi.org/10.5194/acp-16-5283-2016, 2016.

Liu, F., Tao, Z., Beirle, S., Joiner, J., Yoshida, Y., Smith, S. J., Knowland, K. E., and Wagner, T.: A new method for inferring city emissions
and lifetimes of nitrogen oxides from high-resolution nitrogen dioxide observations: a model study, Atmos. Chem. Phys., 22, 1333–1349,
https://doi.org/10.5194/acp-22-1333-2022, 2022.

Lorente, A., Boersma, K., Eskes, H., Veefkind, J., Van Geffen, J., de Zeeuw, M., van der Gon, H. D., Beirle, S., and Krol, M.: Quantification
355   of nitrogen oxides emissions from build-up of pollution over Paris with TROPOMI, Sci. Rep., 9, 1–10, https://doi.org/10.1038/s41598-
019-56428-5, 2019.

Lu, Z., Streets, D. G., de Foy, B., Lamsal, L. N., Duncan, B. N., and Xing, J.: Emissions of nitrogen oxides from US urban areas: estimation
from Ozone Monitoring Instrument retrievals for 2005–2014, Atmos. Chem. Phys., 15, 10367–10383, https://doi.org/10.5194/acp-15-
10367-2015, 2015.

360   Monks, P. S. and Beirle, S.: Applications of Satellite Observations of Tropospheric Composition, in The Remote Sensing of Tropospheric
Composition from Space, edited by J. P. Burrows, P. Borrell, U. Platt, R. Guzzi, U. Platt, and L. J. Lanzerotti, pp. 365–449, Springer Berlin
Heidelberg, [online] Available from: http://www.springerlink.com/content/x66428846gu0870k/abstract/ (Accessed 11 May 2012), 2011.

Pommier, M., McLinden, C. A., and Deeter, M., Relative changes in CO emissions over megacities based on observations from space,
Geophys. Res. Lett., 40, 3766–3771, doi:10.1002/grl.5070, 2013.

365   van Geffen, J. H. G. M., Eskes, H. J., Boersma, K. F., Maasakkers, J. D., Veefkind, J. P.: TROPOMI ATBD of the total and tropospheric
NO_2 data products, S5P-KNMI-L2-0005-RP, Royal Netherlands Meteorological Institute, https://sentinel.esa.int/documents/247904/
2476257/Sentinel-5P-TROPOMI-ATBD-NO_2-data-products, 2019.

van Geffen, J., Eskes, H., Compernolle, S., Pinardi, G., Verhoelst, T., Lambert, J.-C., Sneep, M., ter Linden, M., Ludewig, A., Boersma,
K. F., and Veefkind, J. P.: Sentinel-5P TROPOMI NO_2 retrieval: impact of version v2.2 improvements and comparisons with OMI and
370   ground-based data, Atmos. Meas. Tech., 15, 2037–2060, https://doi.org/10.5194/amt-15-2037-2022, 2022.

Valin, L. C., Russell, A. R., and Cohen, R. C.: Variations of OH radical in an urban plume inferred from NO_2 column measurements,
Geophys. Res. Lett., 40, 1856–1860, doi:10.1002/grl.50267, 2013.

Veefkind, J. P., Aben, I., McMullan, K., Förster, H., de Vries, J., Otter, G., Claas, J., Eskes, H. J., de Haan, J. F., Kleipool, Q., van Weele,
M., Hasekamp, O., Hoogeveen, R., Landgraf, J., Snel, R., Tol, P., Ingmann, P., Voors, R., Kruizinga, B., Vink, R., Visser, H. and Levelt,
375   P. F.: TROPOMI on the ESA Sentinel-5 Precursor: A GMES mission for global observations of the atmospheric composition for climate,
air quality and ozone layer applications, Remote Sensing of Environment, 120, 70–83, doi:10.1016/j.rse.2011.09.027, 2012.

World Emission, ESA project, https://www.world-emission.com/, 2022.